frontiers | Frontiers in Earth Science

TYPE Original Research
PUBLISHED 26 November 2024
DOI 10.3389/feart.2024.1504864

OPEN ACCESS

EDITED BY
Faming Huang,
Nanchang University, China

REVIEWED BY
Jian Ji,
Hohai University, China
Yang Hailong,
Chengdu University of Technology, China
Jianquan Ma,
Xi'an University of Science and Technology, China

*CORRESPONDENCE
Jiangkun He,
13509459051@163.com

RECEIVED 01 October 2024
ACCEPTED 11 November 2024
PUBLISHED 26 November 2024

CITATION
Li R, He J, Zheng H, Zhang C and Zhang S (2024) Early identification on failure mode of loess landslide: insight from case study and physical model experiment.
Front. Earth Sci. 12:1504864.
doi: 10.3389/feart.2024.1504864

Early identification on failure mode of loess landslide: insight from case study and physical model experiment

Ran Li[1,2,3], Jiangkun He[4]*, Han Zheng[4], Chenyuan Zhang[4] and Shuai Zhang[1,2,3]

[1]Institute of Geomechanics, Chinese Academy of Geological Sciences, Beijing, China, [2]Observation and Research Station of Geological Disaster in Baoji, Ministry of Natural Resources, Baoji, Shaanxi, China, [3]Technology Innovation Center for In-situ Stress, Ministry of Natural Resources, Beijing, China, [4]Faculty of Geosciences and Engineering, Southwest Jiaotong University, Chengdu, China

Introduction: The Loess Plateau has long been plagued by cascading loess landslides. The rapid identification of these landslides, along with the accurate determination of their failure modes, is essential for conducting precise disaster assessments in the region. Such assessments are critical for minimizing both human casualties and economic losses. However, the lack of reliable reference data for the early identification of landslide failure modes has resulted in limited detection accuracy, complicating the differentiation between various failure modes. Therefore, investigating the deformation and failure characteristics of loess landslides under different failure modes is crucial for providing a scientific foundation for early hazard detection and the accurate assessment of risk profiles.

Methods: This work examines the pre-slip deformation and post-slip damage characteristics of the rotational-sliding Huzhu Landslide and the translational-sliding Zhongzhai Landslide through a combination of field investigations, unmanned aerial vehicle surveys, and remote sensing interpretation. Physical model tests were conducted to simulate the instability and failure processes of both rotational and translational loess landslides. Meanwhile, three-dimensional models and orthophoto graphic images at various stages of the landslides were generated using Contexcapture.

Results: The initial stages of rotational sliding landslides are marked by the formation of distinct tensile cracks at the trailing edge of the slope and minor uplift at the front. As the uplift at the front progresses and numerous extension fissures develop, the stability of the landslide reduces progressively. Upon reaching instability, the sliding velocity of the sliding mass initially accelerates before decelerating, with majority of the mass remaining on the sliding surface and retaining relatively well structural integrity. At the trailing edge of the landslide, characteristic features such as falling scarps, fractured walls, and sunken grooves can be observed, while the front displays significant bulging phenomena. In contrast, translational sliding landslides are initially characterized by minor tensile cracks at the trailing edge and pronounced deformation at the front. As these tensile cracks propagate, the landslide are prone to sudden instability under external triggering factors. Following the onset of instability, the sliding mass undergoes rapid movement, with only a small part of the mass remaining on the sliding surface.

Discussion: Landslides triggered by different factors and occurring under varying water content conditions may exhibit significant differences in their pre-failure behavior and post-failure characteristics. Thus, it is imperative to conduct further research in this field to better understand these complex dynamics.

KEYWORDS

early identification, rotational landslide, translational landslide, field investigation, physical model test

1 Introduction

Loess in China is primarily concentrated in the northwest, north, and east regions, covering approximately 6.6% of the land area. The loess regions are prone to frequent and diverse geological hazards, resulting in significant economic losses. Among these hazards, loess landslides are among the most widespread and destructive geodisasters. According to statistics, nearly one-third of all landslides nationwide occur in loess regions (Peng et al., 2019; Saleem et al., 2019). Recently, the increasing frequency of loess landslides has been linked to intensified human engineering activities and the northward shift of the equal precipitation line in China, with rotational and translational sliding being the most common failure modes (Zhang and Li, 2011). Despite extensive research on the distribution characteristics, developmental patterns, causes, and mechanisms of loess landslides (Zhu et al., 2013; Lan et al., 2021; Yao et al., 2022), identifying potential landslide hazards remains a difficulty for researchers due to the unique properties of loess (Peng et al., 2020). Landslide identification is the foundation for landslide risk assessment and other related studies (Tie et al., 2022; Wang et al., 2024). It is estimated that 80% of landslides occur outside the existing catalog, with only less than 1% of the world's areas being cataloged for landslides (Brabb, 1991; Zhang Q. et al., 2022; Shao et al., 2022). Rapid identification of potential landslide hazards not only reduces casualties and economic losses but also enables precise analysis of landslide risks in loess regions.

In the early stages, the identification of potential landslides was primarily achieved through field investigations conducted by researchers, which requires substantial time, manpower, and financial resources when dealing with large numbers of landslides distributed over wide areas (Dou et al., 2023). With the advancement of remote sensing technology, which provides rich information, rapid data acquisition, and extensive coverage, the limitations of field surveys have been effectively mitigated, leading to its increasing application in landslide identification. For example, after the landslide in Xinmo Village, Maoxian County, Sichuan Province, in 2017, which involved a high elevation and invisibility, the development of a "three-step" integrated system for potential landslide identification was proposed, encompassing satellite, aerial, and ground-based monitoring (Xu, 2018; Xu et al., 2019). This approach highlighted the critical role that comprehensive remote sensing technologies can play in geological hazard investigations (Ge, 2018; Ge et al., 2019; Li et al., 2019; Zhang et al., 2018; Dong et al., 2018a; Dong et al., 2018b; Zhao et al., 2019; Lu et al., 2019; Xu, 2020; Guo et al., 2021; Huang et al., 2024a). However, the previous studies on landslide hazard identification have predominantly focused on determining whether a landslide will occur based on detecting deformation indicators. In contrast, research on using these indicators and damage characteristics to predict failure modes remains limited. Since landslides with different failure modes exhibit significantly varying disaster-causing potentials, using landslide hazard identification to predict failure modes is of great significance for disaster prevention and mitigation.

This study focuses on two typical loess landslide events. Through field investigations and physical model experiments, it examines the pre-sliding deformation characteristics and post-sliding failure features under different failure modes of loess landslides. The findings provide a reference for further research on the identification of potential hazards related to landslide failure modes.

2 Case study

The failure modes of loess landslides typically include rotational sliding and translational sliding. Significant differences exist in the landslide characteristics and the extent of the hazard under different failure modes. This section selects two case studies for analysis: a rotational sliding instability loess landslide that occurred on 1 September 2022, in Huzhu County, Qinghai Province, China, and a translational sliding instability loess landslide that occurred on 5 October 2021, in Niangniangba Town, Gansu Province, China. The deformation and failure characteristics of loess landslides under these two failure modes are summarized, providing criteria for identifying potential hazards of loess landslides and determining their failure modes.

2.1 Huzhu landslide

At 1:05 a.m. on 1 September 2022, the Huzhu landslide occurred on the northwest side of Hongya Village, Weiyuan Town, Huzhu County, Qinghai Province, resulting in seven fatalities and an estimated direct economic loss of 85.51 million RMB. The Huzhu landslide (101°56′3.00″E; 36°51′41.04″N) developed in the transitional zone between the low mountains and hilly areas on the right bank of the Nanmenxia River and the adjacent river valley plain, northwest of Hongya Village. The landslide's overall planform resembles a "broad tongue" shape (Figure 1A), with the primary sliding direction ranging from 103° to 167°. The trailing edge of the landslide lies at an elevation between 2726.0 and 2666.0 m, while the front edge sits at an elevation between 2547.0 and 2580 m, yielding a total vertical drop of 114–152 m. The landslide measures approximately 370–740 m in length and

FIGURE 1
Overview of the Huzhu landslide. Planar view of the Huzhu landslide **(A)**. Slip cliff **(B)**. Shingled terrain **(C)**. Tension sunk grooves **(D)**. Trailing-edge cracks **(E)**. Reverse-slope terrain **(F)**. Bulging cracks **(G)**.

470–1,050 m in width, covering an area of about 53.2×10^4 m^2. With an average thickness of around 40 m, the Huzhu landslide has an estimated volume of approximately 2108 $\times10^4$ m^3, and it belongs to a huge landslide. After the Huzhu landslide occurred, four secondary landslides formed, covering areas of 25,700 m^2 (1#), 97,300 m^2 (2#), 13,100 m^2 (3#), and 90,900 m^2 (4#) (Figure 1A). The initial slope failure began as early as 17:00 (UTC +8) on 31 August 2022, with the 1# landslide occurring in a slow-moving state and impacting the driving school at the foot of the hill. Subsequently, the 2#, 3#, and 4# landslides occurred around 1:05 (UTC +8) on 1 September 2022. The primary triggering factor was the intense rainfall experienced in August, which initiated the landslides (Zhang et al., 2023).

The Huzhu landslide has an overall armchair-like shape with well-defined boundaries on all sides. The slip cliff at the trailing edge of the landslide extends approximately 480 m and forms a curved steep face (Figure 1B), with slopes typically ranging from 60° to 70° and heights between 8 and 40 m. The sliding movement at the trailing edge has formed a distinct shingled terrain (Figure 1C). The slope surface is characterized by well-developed shear scarps and cracks (Figure 1A), along with numerous sunk scarps, slip cliffs, and tension grooves (Figures 1D, E). The heights of the shear scarps, cliffs, and natural step-like scarps typically vary between 3 and 5 m, while the tension grooves are generally 2–4 m deep and 3–5 m wide. The overall displacement of the landslide is relatively small (9 m), and the landslide mass remains largely intact, retaining its original slope profile and forming a stepped appearance (Figure 2). A noticeable reverse-slope terrain can be observed in the mid-to-rear section (Figure 1F). The eastern boundary at the front exhibits a series of swelling deformations, with the surface development of bulging cracks (Figure 1G). These characteristics further confirm that the Huzhu landslide is a rotational landslide.

According to the research report provided by the local government, prior to July 2022, the cumulative deformation of the Huzhu landslide was relatively minor, ranging from approximately −30 mm–60 mm. However, after July 2022 (about 2 months before the landslide occurred), the cumulative displacement exhibited a more pronounced pattern: at the rear of the landslide, displacements ranged from −120 mm to −60 mm; in the middle, from −60 mm to −30 mm; and at the front, from 30 mm to 90 mm. This deformation pattern was characterized by subsidence at the rear, sliding in the middle, and uplift at the front. Interestingly, despite these changes, no significant deformation signs were detected in the historical imagery available (Figure 3). Prior to the landslide failure, deformation increased in the front and rear part of the sliding mass, and the extent of internal deformation expanded. Overall, the landslide exhibited a complex deformation failure pattern: initial creeping deformation at the front, followed by deformation in the middle and rear. Deformation in the rear part of the landslide exerted pressure, pushing the middle and front sections, manifesting a combination of front-end traction and rear-end thrust (Zhang et al., 2023).

2.2 Zhongzhai landslide

The Zhongzhai landslide occurred in the early morning of 5 October 2021,burying and destroying the houses and courtyards of two households located at the foot of the slope, as well as damaging farmland in the area. The economic loss is estimated at approximately 500,000 RMB. The Zhongzhai landslide (105°47′59″E; 34°17′59″N) developed on the hilly slope north of Zhongzhai Village. The landslide has a bottleneck shape in plain view, being wider at the front and trailing edge and narrower in the middle (Figure 4A). The main sliding direction is 183°, with a

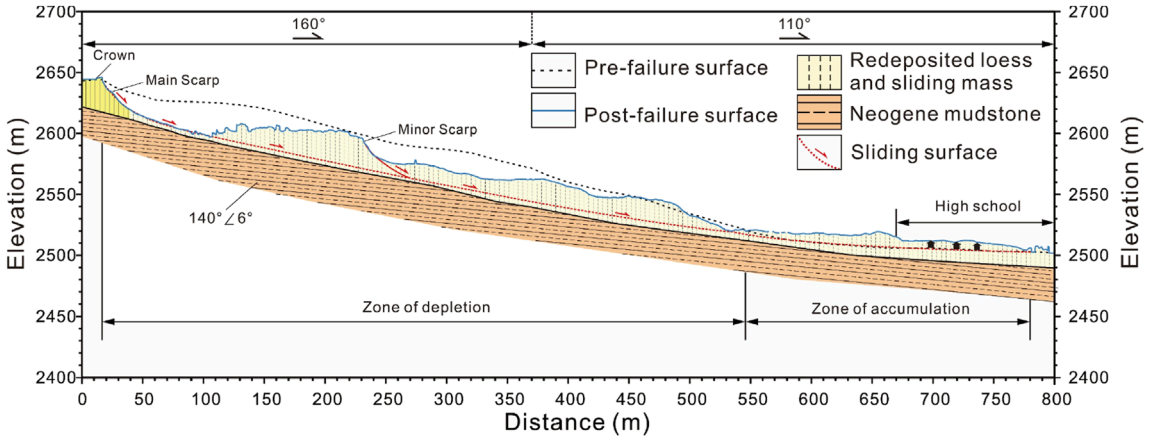

FIGURE 2
Profile of the Huzhu landslide.

vertical height difference of about 70 m from the top to the foot of the slope. The average width of the landslide is approximately 150 m, and its axial length is about 150 m, covering a plan area of 22×10^3 m^2. The average thickness of the landslide is approximately 3 m, with a total volume of about 67.5×10^3 m^3, being classified as a small-scale landslide. Furthermore, from October 2 to 5, the landslide area experienced continuous heavy rainfall. The substantial infiltration of rainwater increased the weight of the slope and reduced the shear strength of the sliding layer, ultimately triggering the landslide.

The eastern and western boundaries of the landslide are clearly defined, with no significant differences in terrain, both demarcated by the slope itself. The slip cliff on the northern trailing edge of the landslide is mainly defined by a grooved terrain (Figure 4B), with a noticeable elevation difference between the trailing edge and the surrounding area. Distinct tension cracks are visible along the slip cliff (Figure 4C). The slope of the landslide ranges from 30° to 40°, with the trailing edge forming a steep slope and the front edge presenting a gentler slope. The slope surface is relatively straight. The sliding velocity was relatively high during the landslide movement, resulting in a smooth sliding surface (Figure 4D). Additionally, most of the sliding mass accumulated at the foot of the slope, leaving little debris in the channel (Figure 4E).

The Zhongzhai landslide is a typical loess-bedrock interface landslide, with the sliding surface at the interface between the underlying silty slate and the overlying Malan loess (Figure 5). Analysis of historical satellite imagery (Figure 6) reveals that a previous landslide occurred in the study area in 2013. Before the 2013 Zhongzhai landslide, a small valley was visible at the lower slope, while the upper slope remained relatively intact (Figure 6A). During a heavy rainstorm in June 2013, the slope experienced sliding and buried four houses. An abandoned road can be seen at the foot of the slope after the 2013 landslide (Figure 6B). From 2013 to 2019, there were no signs of significant deformation in the Zhongzhai landslide area (Figures 6B–D). The vegetation growth on the slope indicates that rainfall during this period was sufficient for plant growth but not enough to trigger further landslides. In Figure 6E, tension cracks appeared at the top of the main scarp, indicating that failure was gradually evolving. In October 2021, after a heavy rainstorm, the slope failed again (Figure 6F). Based on high-resolution topographic data, multi-temporal orthophotos, and field investigations, it is concluded that the tension cracks at the top of the main scarp in 2020 extended under prolonged infiltration from heavy rainfall, eventually leading to crack penetration and rapid slope destabilization (Zhang S. et al., 2022).

Due to various limitations during the field investigation and the possibility that the original deformation signs of the landslide may have been covered after landslide occurrence, the inquiry may have yet to capture the deformation and failure characteristics of the landslide fully. In recent years, many researchers have gradually improved and favored the model test method (Hu et al., 2023; Fang et al., 2023a; Fang et al., 2023b). Therefore, through indoor physical model experiments, this study will further explore the deformation and failure characteristics of rotational sliding and translational sliding in loess landslides.

3 Physical model tests

Rotational sliding and translational sliding loess landslides are two major typical landslide types in the northwest region of China. Although the signs of failure may vary due to factors such as topography, these two types of landslides exhibit some common failure characteristics due to the differences in their failure modes. To investigate the early failure characteristics of both rotational and translational loess landslides, this work designs model experiments for each type of landslide to reveal their early-stage failure behaviors. By rigorously comparing the experimental results with the previously discussed case studies (Huzhu rotational landslide and Zhongzhai translational landslide), the study summarizes the early identification markers for both rotational and translational landslides, ensuring the validity and reliability of the findings. It is

FIGURE 3
Historical deformation process of the Huzhu landslide.

important to note that the model experiments for these two types of landslides are not based on specific case studies, but rather are designed to reflect the characteristics of the two distinct landslide failure modes. The ultimate goal is to apply these findings to identify potential loess landslide hazards. At the start of the experiment, one end of the slope model is gradually lifted at a uniform speed using a lifting device. Once the slope reaches a certain angle, it can destabilize and slide according to the pre-set sliding mode. During the test, deformation signs of the landslide at different stages are captured, and the images are imported into ContextCapture for 3D modeling. This process yields a 3D model and orthophotos of the landslide for further analysis. The specific testing process is outlined as follows.

3.1 Sample collection and soil properties

The loess (Malan loess) used for the model experiment was collected from the Zhongzhai landslide. Through laboratory tests, the physical and mechanical properties of the loess were studied, and the results are presented in Table 1. Additionally, the particle size distribution of the loess was obtained (Figure 7).

3.2 Model preparation

The soil samples collected from the field were crushed and sieved through a 2 mm mesh, then dried (at 105°C for 24 h). The

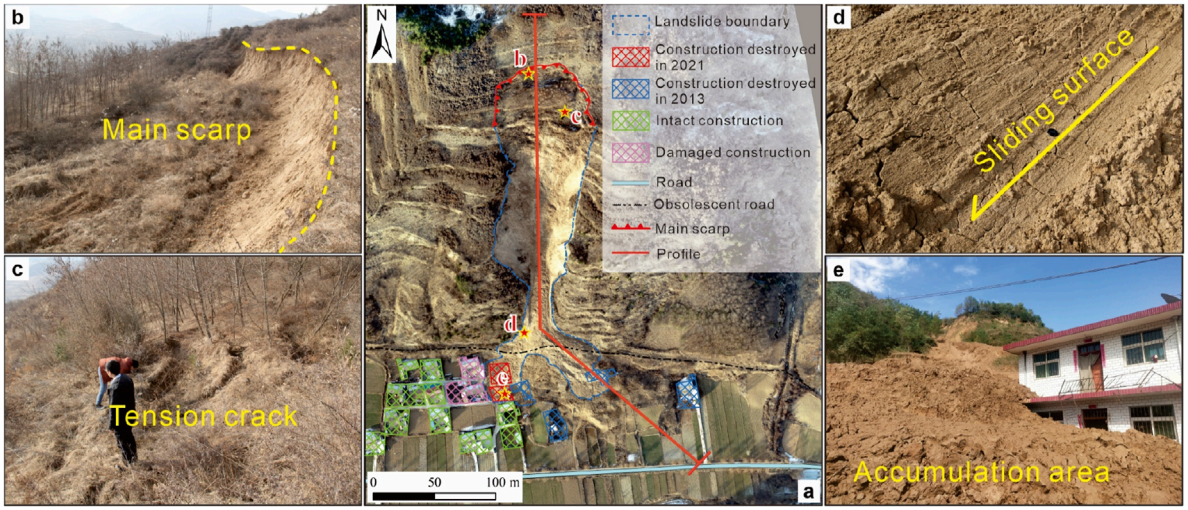

FIGURE 4
Overview of the Zhongzhai landslide. Planar view of the Zhongzhai landslide **(A)**. Slip cliff **(B)**. trailing-edge cracks **(C)**. Sliding striation **(D)**. Front edge of the landslide **(E)**.

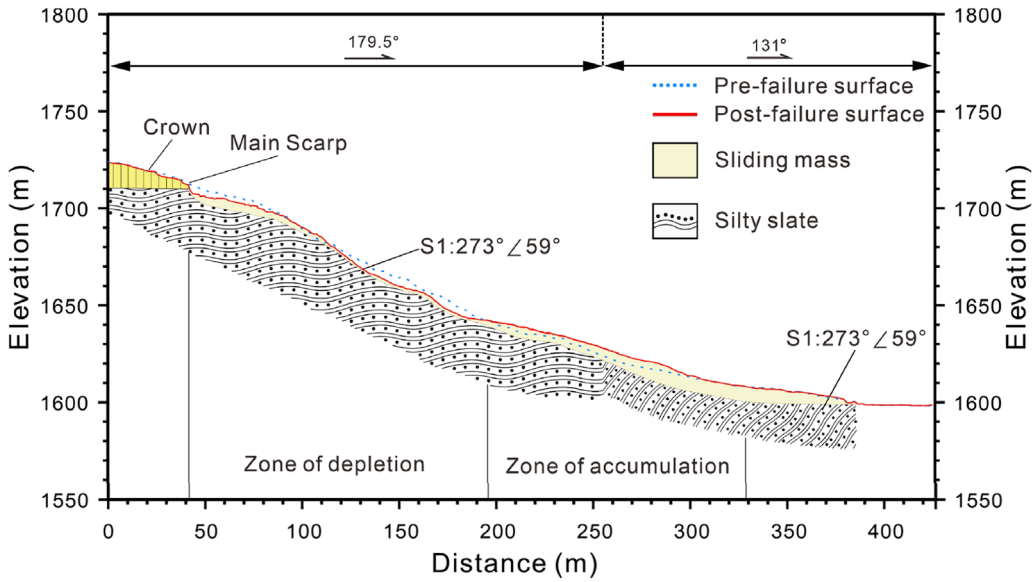

FIGURE 5
Profile of the Zhongzhai landslide.

experimental materials were prepared according to the natural moisture content of the loess slope in the field for use in the model experiment. The physical model test was conducted using an acrylic box with internal dimensions of 80 cm in length and 40 cm in width, which was applied to build the loess slope. The side walls of the model box are constructed from highly polished glass, ensuring that the experiment is unaffected by any external interference. Through preliminary experimentation, the slope model was designed with a height of 22.5 cm. Loess with a total mass of 94 kg was then filled into the model box in layers and compacted. After the final compaction, the loess reached the designed model height. At this point, the density of the slope model was 1.3 g/cm^3, closely approximating the natural density of loess slopes (Figure 8A), which closely approximates the density of natural loess slopes. Considering the smooth nature of Teflon film, it was used as the sliding surface material. The slope model was then excavated to create a flat or circular sliding surface (Figures 8B, C). The depth of the curved sliding surface was approximately 3.4 times the depth of the shallow sliding surface. The Teflon film was laid on the excavated sliding surface, after which the loess was backfilled, and the surface of the slope model was leveled. As a result, two typical slope models with different failure modes were

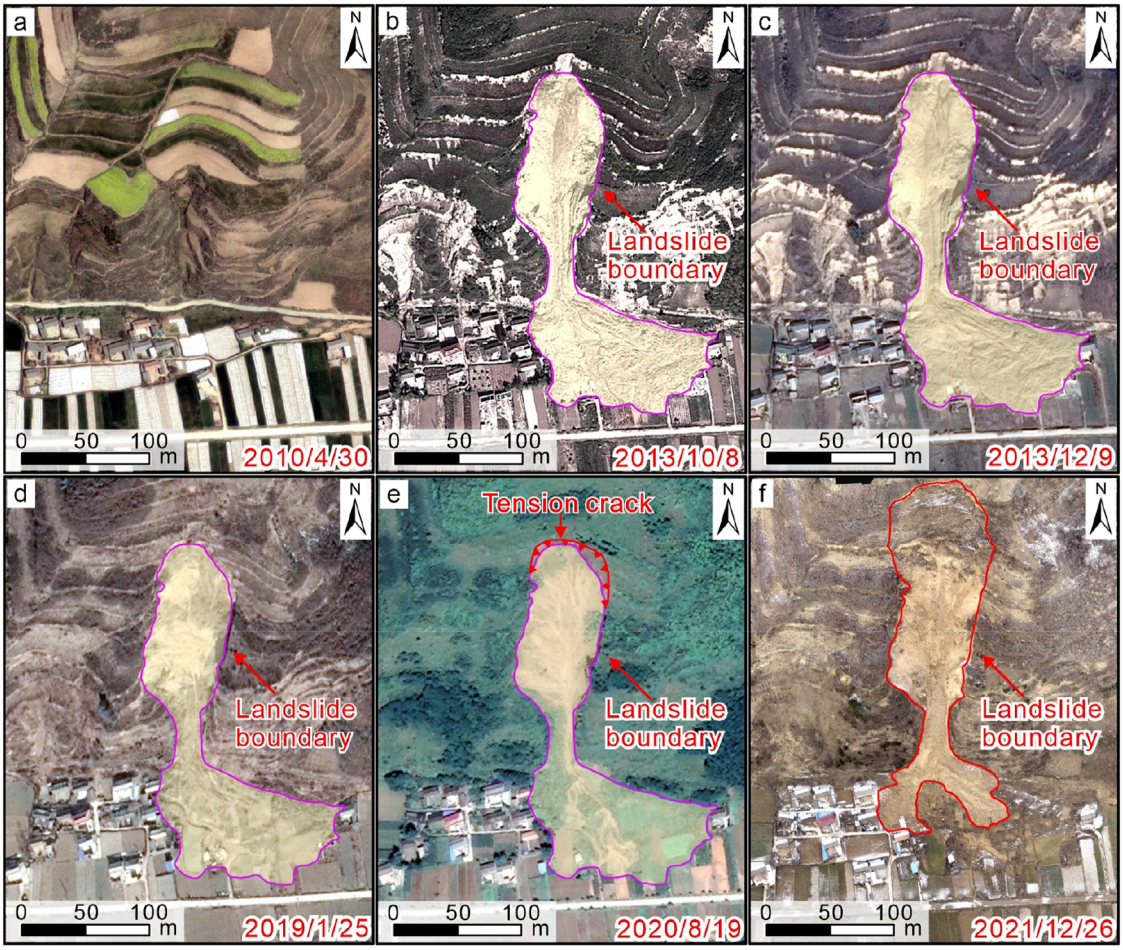

FIGURE 6
Historical deformation process of the Zhongzhai landslide.

TABLE 1 The physical properties of loess samples.

Natural moisture content	Density	Gravity	Liquid limit (%)	Plastic limit (%)	Plastic index
2.1%	1.22 g/cm^3	2.78	31.2	14.9	16.3

obtained: rotational sliding failure mode and translational sliding failure mode.

3.3 Test process and data collection

In order to study the deformation and failure characteristics of slope failure at different stages, eight camera positions were set up around the model box (Figure 9) to capture image data from various angles simultaneously. This setup allowed for a comprehensive analysis of surface deformation during the slope failure (Wen et al., 2017; Zhang et al., 2021; Zhang et al., 2024a). The specific steps are outlined as follows. Before the experiment, all smartphones were set to the same camera resolution (1080p/60fps) and positioned parallel to the slope surface above the model box (Figure 9), ensuring that the orthophoto of the slope could be captured. This arrangement allowed for a certain degree of overlap among the images from the various phones, ensuring complete coverage of the slope surface. Once the experiment commenced, a hand winch was used to slowly and uniformly elevate the model box. During this process, the eight Android phones were connected to a control software on a computer, enabling simultaneous capture of images at different stages of the landslide. Each capture session yielded eight images at once. The model box was raised until instability and failure occurred, at which point the elevation was halted. The images obtained during the experiment were then imported into ContextCapture for modeling, resulting in a three-dimensional model and orthophotos of the landslide at various stages for further analysis. Both trials were conducted following this procedure.

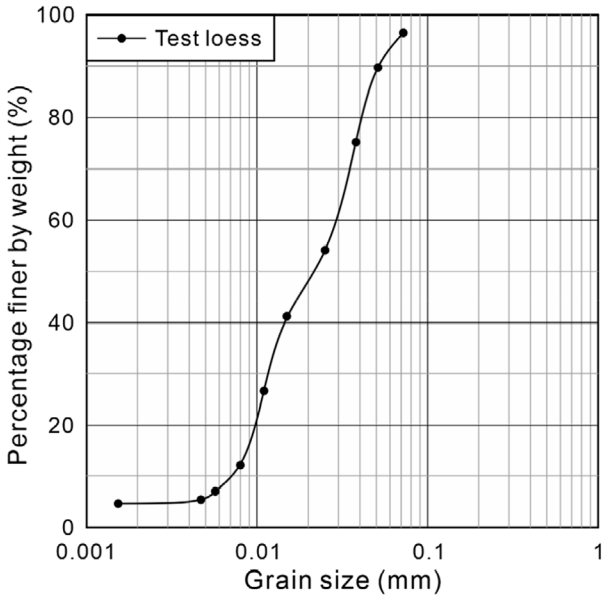

FIGURE 7
Particle size distribution curve of the loess sample.

3.4 Analysis of landslide failure characteristics

During the slope test for rotational sliding, failure occurred when the model box was tilted to an angle of 44°. As shown in Figure 10A, the slope model after rotational sliding failure exhibits a distinct arcuate steep scarp with a slope angle ranging from 60° to 70°. In the middle to rear portion of the landslide, a reversed platform develops, accompanied by numerous shear cracks, and a depression forms in the trailing edge of the landslide (Figure 10B). Although the landslide mass is not completely disintegrated, its internal structure is significantly damaged. The landslide mass fully disintegrates at the shear outlet and gradually accumulates downslope. The topographic features reveal a notable depression in the middle and rear portions of the landslide, while the front experiences severe uplift (as shown in Figure 10C). The entire landslide mass moves downslope toward the foot of the slope, with the slope gradient exhibiting a marked anti-dip characteristic compared to the original slope, with an anti-dip angle ranging from 3° to 8° (Figure 10C).

During the slope test for translational sliding, failure occurred when the model box was tilted to an angle of 37°. The mode of slope failure is illustrated in Figure 11A. Small cracks initially appear at the rear of the slope as the model is uplifted, while no significant indications of deformation are observed in other areas of the slope. As the rear cracks propagate and eventually penetrate through, the soil mass at the front of the landslide rapidly disintegrates and slides downward. The remaining landslide mass quickly exits the shear outlet and accumulates at the lower part of the slope. The rear of the landslide forms a steep slope, while the front slope presents a gentle, relatively straight surface (Figures 11B, C).

3.5 Analysis of differences between rotational and translational landslide

To investigate the differences in failure mechanisms of landslides under various modes, a graph was created to illustrate the relationship between slope angle and soil deformation. The results indicate that during translational sliding, once the rear cracks fully penetrate (Figure 12A) and the crack width reaches only 0.3 mm, the front of the landslide begins to deform rapidly, exhibiting sliding behavior (Figure 12A). This instability occurs before any further changes in the slope angle, causing the slope failure and the rapid slide and plunge downward of the sliding mass (Figure 12B). In contrast, even after the rear cracks penetrate and the crack width reaches approximately 1 mm for rotational landslide, the front of the slope exhibits bulging without any immediate sliding of the soil mass (Figure 12C). As the slope angle increases, the slope

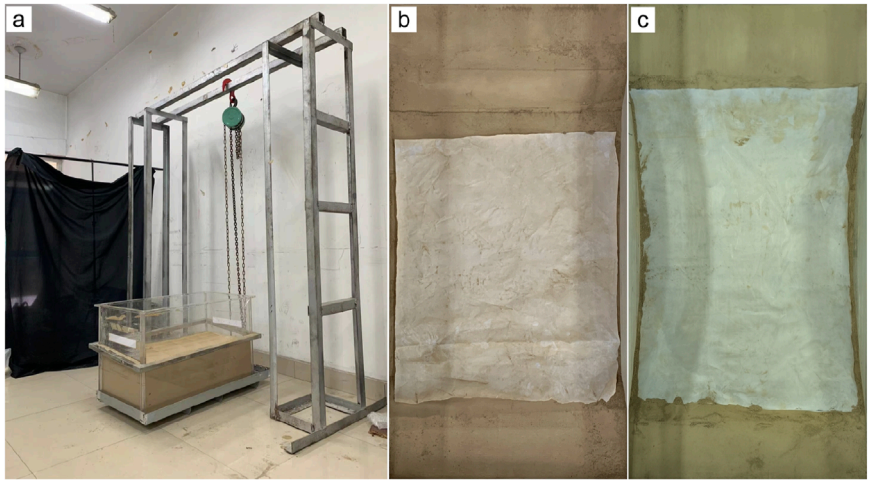

FIGURE 8
Physical model test preparation. Experimental device **(A)**. Flat sliding surface **(B)**. Circular sliding surface **(C)**.

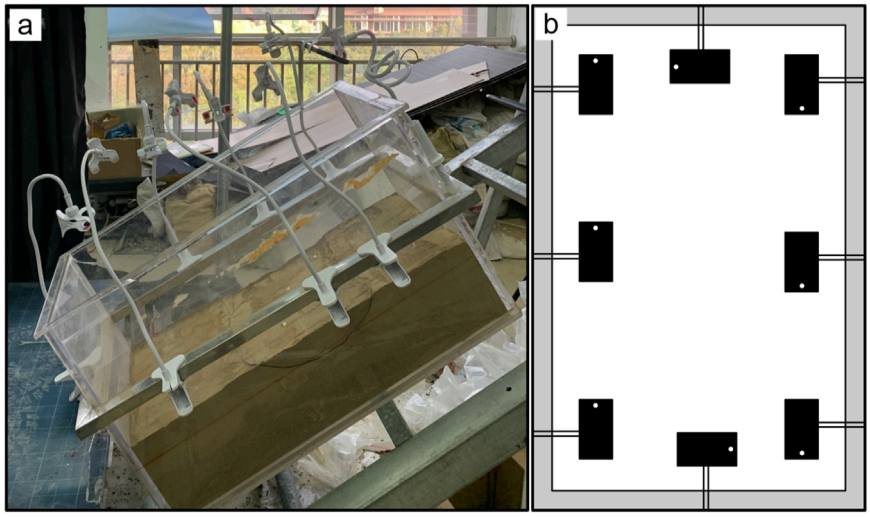

FIGURE 9
Experimental data acquisition system. Physical device diagram **(A)**. Mobile phone location diagram **(B)**.

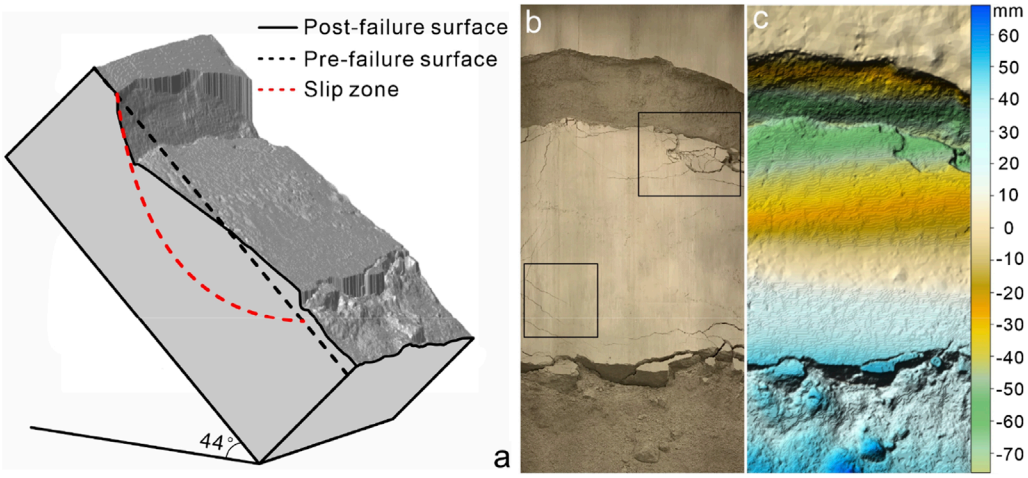

FIGURE 10
Rotational landslide. 3D model **(A)**. Image after landslide failure **(B)**. The terrain undulation after landslide damage **(C)**.

ultimately experiences instability and failure (Figure 12D). However, the integrity of the landslide mass remains relatively intact, and the sliding during the failure process occurs more gradually. In addition, the deformation of the sliding mass gradually becomes slow when the slope angle stops increasing (Figure 12E). It indicates that rotational sliding landslides tend to exhibit a slower and more gradual failure process in the absence of external triggering forces.

4 Discussion

The current research on landslide hazard identification often needs a unified reference basis, leading to divergent interpretations of the same hazard point by individuals from different professional backgrounds. Meanwhile, many uncertainties exist in predicting landslide susceptibility (Chang et al., 2023; Huang et al., 2024b; Huang et al., 2024c; Zhang et al., 2024a; Zhang et al., 2024b). Furthermore, there needs to be more understanding of assessing failure modes based on identifiable landslide deformation and failure characteristics. Through field investigation, this study investigates the deformation and failure features of loess landslides under two distinct failure modes. It successfully simulates the instability process by physical model tests, which refines the deformation and failure characteristics associated with different failure modes. This work can provide a basis for identifying landslide failure modes through hazard recognition. For rotational sliding loess landslides, early deformation is marked by the formation of distinct tensile cracks perpendicular to the slope direction at the rear of the slope, while minor bulging is observed at the front of the slope. Even after the rear crack penetrates through the slope,

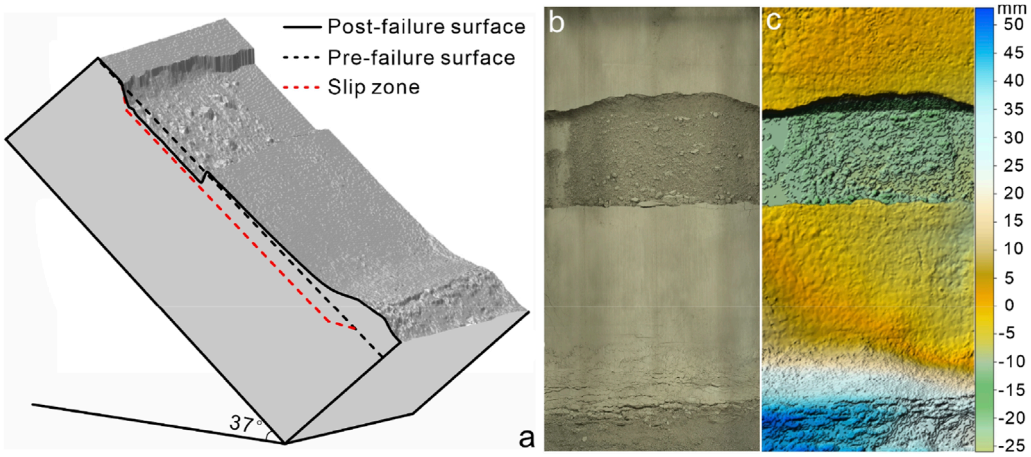

FIGURE 11
Translational landslide. 3D model **(A)**. Orthograph after landslide failure **(B)**. The terrain undulation after landslide damage **(C)**.

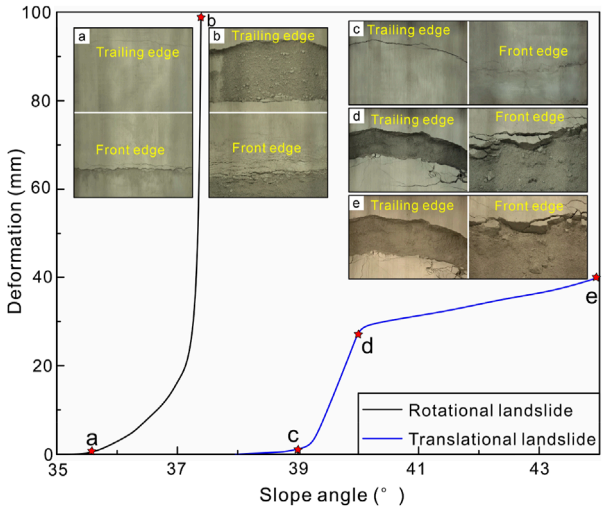

FIGURE 12
Slope deformation process of landslides in two failure modes.

instability has not yet occurred. As deformation progresses, the bulging at the front of the slope develops numerous bulging cracks, leading to partial front disintegration and eventual slope failure. After the landslide occurs, a significant portion of the mass typically remains on the sliding bed with good integrity. Rear features include shingle-like topography, while the middle to rear sections of the slope display distinct anti-slope formations, with shear scarps and well-developed cracks, forming numerous steep scarps, slip cliffs, and grooves. Bulging phenomena are prominent at the front of the landslide. The sliding speed of the landslide mass in rotational sliding typically shows an initial increase followed by a decrease.

In translational sliding loess landslides, the appearance of small tensile cracks at the trailing edge of the slope, along with noticeable deformation at the front, serves as an early warning sign of potential failure. As deformation progresses and rear cracks penetrate through the slope, the soil mass at the front gradually disintegrates, followed by rapid sliding as the landslide mass exits through the shear outlet, leading to overall slope instability. The presence of penetrating rear cracks is a critical indicator of imminent translational sliding failure in loess landslides. Post-failure, the landslide mass mostly accumulates at the foot of the slope, with little mass remaining in the channel, and tensile cracks parallel to the rear wall are observable.

The failure process of the translational sliding observed in the experiments closely mirrors real-world cases. However, there are significant discrepancies in the failure process of the rotational sliding compared to the mutual assistance landslide documented in the case study. The mutual assistance landslide, triggered by continuous rainfall, exhibited phenomena such as initial sliding followed by flow and movement liquefaction, leading to rapid movement after instability. This contrasts with the experimental observations of rotational sliding, where the sliding speed initially increased before subsequently decreasing. Despite these differences, the early deformation and failure characteristics of both types of landslides are largely consistent. This suggests that landslides induced by various factors, such as rainfall or earthquakes, can exhibit pronounced differences in their post-failure movement dynamics, highlighting the need for further research in this area.

Furthermore, several preliminary experiments with varying moisture content levels were conducted in this study. However, the method of inducing slope deformation and failure through rotational elevation revealed significant limitations. When the moisture content was high, the cohesive properties of the loess effectively prevented any visible deformation in the slope model, even when the model box was rotated to its maximum angle. Although a sliding surface was pre-established within the slope, the model maintained its overall integrity and did not exhibit failure. After evaluating multiple slope models with different moisture contents, a model with a moisture content of 2.1% was selected for the main experiments due to its clear

signs of deformation and comprehensive failure characteristics. However, it is important to note that the deformation and failure features of slope models at varying moisture levels exhibited some differences, indicating the need for further investigation in this area.

5 Conclusion

This paper systematically investigates the deformation and failure characteristics of rotational and translational sliding loess landslides through a combination of case studies and physical model experiments. The study provides a basis for early identification and assessment of landslide failure modes in loess regions, leading to the following conclusions:

1. The early signs of rotational sliding in loess landslides are characterized by the presence of distinct tensile cracks at the trailing edge and minor bulging at the front edge. Obvious bulging at the front and numerous bulging cracks parallel to the slope indicate an impending rotational sliding event. After the landslide occurs, a significant portion of the sliding mass remains on the sliding surface with relatively good integrity. Features such as sunk scarps, slip cliffs, and tension-falling grooves at the trailing edge are evident. At the same time, bulging phenomena are prevalent at the front, serving as typical indicators of rotational loess landslide occurrence.
2. Early indicators of translational sliding include small tensile cracks at the trailing edge and significant deformation at the front. The progressive disintegration of the front soil mass and the penetration of rear cracks, signals an imminent landslide. After the landslide, most of the sliding mass accumulates at the foot of the slope, and tensile cracks parallel to the slip cliff become visible, typical post-failure indicators of translational loess landslides.
3. In a rotational sliding landslide, the sliding mass exhibits a velocity trend of increasing initially and then decelerating after its initial slope failure. The sliding velocity of the sliding mass of the translational sliding landslide is fast after its initial slope failure and this kind of landslide features an abrupt occurrence.

Data availability statement

The original contributions presented in the study are included in the article/supplementary material, further inquiries can be directed to the corresponding author.

Author contributions

RL: Funding acquisition, Investigation, Methodology, Supervision, Validation, Writing–original draft. JH: Data curation, Investigation, Validation, Writing–original draft. HZ: Investigation, Writing–review and editing. CZ: Investigation, Methodology, Writing–review and editing. SZ: Writing–review and editing.

Funding

The author(s) declare that financial support was received for the research, authorship, and/or publication of this article. This work was financially supported by the National Natural Science Foundation of China (42207234 and 42302333), and the Fundamental Science Foundation of Institute of Geomechanics (DZLXJK202306).

Conflict of interest

The authors declare that the research was conducted in the absence of any commercial or financial relationships that could be construed as a potential conflict of interest.

Generative AI statement

The author(s) declare that no Generative AI was used in the creation of this manuscript.

Publisher's note

References

Brabb, E. E. (1991). The world landslide problem. *Episodes J. Int. Geoscience* 14 (1), 52–61. doi:10.18814/epiiugs/1991/v14i1/008

Chang, Z., Huang, F., Huang, J., Jiang, S., Liu, Y., Meena, S. R., et al. (2023). An updating of landslide susceptibility prediction from the perspective of space and time. *Geosci. Front.* 14 (5), 101619. doi:10.1016/j.gsf.2023.101619

Dong, J., Liao, M., Xu, Q., Zhang, L., Tang, M., and Gong, J. (2018a). Detection and displacement characterization of landslides using multi-temporal satellite SAR interferometry: a case study of Danba County in the Dadu River Basin. *Eng. Geol.* 240 (5), 95–109. doi:10.1016/j.enggeo.2018.04.015

Dong, J., Zhang, L., Tang, M., Liao, M., Xu, Q., Gong, J., et al. (2018b). Mapping landslide surface displacements with time series SAR interferometry by combining persistent and distributed scatterers: a case study of Jiaju landslide in Danba, China. *Remote Sens. Environ.* 205, 180–198. doi:10.1016/j.rse.2017.11.022

Dou, H., Huang, S., Jian, W., and Wang, H. (2023). Research on rapid identification technology of highway landslide in Mountainous areas of southeast Fujian based on remote sensing data. *J. Nat. Disasters* 32 (1), 217–227. (in Chinese with English abstract). doi:10.13577/j.jnd.2023.0124

Fang, K., Miao, M., Tang, H., Jia, S., Dong, A., An, P., et al. (2023a). Insights into the deformation and failure characteristic of a slope due to excavation through multi-field

monitoring: a model test. *Acta Geotech.* 18 (2), 1001–1024. doi:10.1007/s11440-022-01627-0

Fang, K., Tang, H., Li, C., Su, X., An, P., and Sun, S. (2023b). Centrifuge modelling of landslides and landslide hazard mitigation: a review. *Geosci. Front.* 14 (1), 101493. doi:10.1016/j.gsf.2022.101493

Ge, D. (2018). Integrated remote sensing application in early identification, monitoring of geological hazards. *City Disaster Reduct.* 6, 53–60. (in Chinese). doi:10.3969/j.issn.1671-0495.2018.06.011

Ge, D., Dai, K., Guo, Z., and Li, Z. (2019). Early identification of serious geological hazards with integrated remote sensing technologies: thoughts and recommendations. *Geomatics Inf. Sci. Wuhan Univ.* 44 (7), 949–956. (in Chinese with English abstract). doi:10.13203/j.whugis20190094

Guo, C., Xu, Q., Dong, X., Liu, X., and She, J. (2021). Geohazard recognition by airborne LiDAR technology in complex mountain areas. *Geomatics Inf. Sci. Wuhan Univ.* 46 (10), 1538–1547. (in Chinese with English abstract). doi:10.13203/j.whugis20210121

Hu, Y., Ji, J., Sun, Z., and Dias, D. (2023). First order reliability-based design optimization of 3D pile-reinforced slopes with Pareto optimality. *Comput. Geotechnics* 162, 105635. doi:10.1016/j.compgeo.2023.105635

Huang, F., Li, R., Catani, F., Zhou, X., Zeng, Z., and Huang, J. (2024a). Uncertainties in landslide susceptibility prediction: influence rule of different levels of errors in landslide spatial position. *J. Rock Mech. Geotechnical Eng.* 16, 4177–4191. doi:10.1016/j.jrmge.2024.02.001

Huang, F., Mao, D., Jiang, S. H., Zhou, C., Fan, X., Zeng, Z., et al. (2024b). Uncertainties in landslide susceptibility prediction modeling: a review on the incompleteness of landslide inventory and its influence rules. *Geosci. Front.* 101886, 101886. doi:10.1016/j.gsf.2024.101886

Huang, F., Teng, Z., Yao, C., Jiang, S. H., Catani, F., Chen, W., et al. (2024c). Uncertainties of landslide susceptibility prediction: influences of random errors in landslide conditioning factors and errors reduction by low pass filter method. *J. Rock Mech. Geotechnical Eng.* 16 (1), 213–230. doi:10.1016/j.jrmge.2023.11.001

Lan, H., Zhu, Y., Li, L., Pan, T., Hu, Z., and Peng, J. (2021). Multi process interaction of geology, geomorphology and climate in the Yellow River Basin and its gestation mechanisms on major disasters. *Bull. Natl. Nat. Sci. Found. China* 28 (2), 257–267. (in Chinese with English abstract). doi:10.16262/j.cnki.1000-8217.2021.04.003

Li, Z., Song, C., Yu, C., Xiao, R., Chen, L., Luo, H., et al. (2019). Application of satellite radar remote sensing to landslide detection and monitoring: challenges and solutions. *Geomatics Inf. Sci. Wuhan Univ.* 44 (7), 967–979. (in Chinese with English abstract). doi:10.13203/j.whugis20190098

Lu, H., Li, W., Xu, Q., Dong, X., Dai, C., and Wang, D. (2019). Early detection of landslides in the upstream and downstream areas of the Baige Landslide, the Jinsha River based on optical remote sensing and InSAR technologies. *Geomatics Inf. Sci. Wuhan Univ.* 44 (9), 1342–1354. (in Chinese with English abstract). doi:10.13203/j.whugis20190086

Peng, J., Wang, Q., Men, Y., Xu, Q., and Zhuang, J. (2019). *Landslide disasters in the loess plateau*. Beijing: Science Press.

Peng, J., Wang, Q., Zhuang, J., Leng, Y., Fan, Z., and Wang, S. (2020). Dynamic formation mechanism of landslide disaster on the Loess Plateau. *J. Geomechanics* 26 (5), 714–730. (in Chinese with English abstract). doi:10.12090/j.issn.1006-6616.2020.26.05.059

Saleem, N., Huq, M. E., Twumasi, N. Y. D., Javed, A., and Sajjad, A. (2019). Parameters derived from and/or used with digital elevation models (DEMs) for landslide susceptibility mapping and landslide risk assessment: a review. *ISPRS Int. J. Geo-Information* 8 (12), 545. doi:10.3390/ijgi8120545

Shao, Y., Zhang, M., and Xie, C. (2022). Present situation and prospect of comprehensive monitoring in geological hazard by remote sensing. *Geol. Resour.* 31 (3), 381–394. (in Chinese with English abstract). doi:10.13686/j.cnki.dzyzy.2022.03.014

Tie, Y., Xu, W., Xiang, B., Lu, J., Gong, L., Gao, Y., et al. (2022). The thoughts on construction of "double–control of point and zone" system of geological hazard risk in southwest China. *Chin. J. Geol. Hazard Control* 33 (3), 106–113. (in Chinese with English abstract). doi:10.16031/j.cnki.issn.1003-8035.2022.03-12

Wang, G., Li, G., Sun, X., Li, H., Tian, Y., Dong, H., et al. (2024). Preliminary study on the "point–surface dual control" model of geological hazard risk in typical mountainous towns in Gansu Province. *Geol. China*, 1–21. (in Chinese with English abstract). doi:10.12019/gc20230220001

Wen, T., Tang, H., Wang, Y., Lin, C., and Xiong, C. (2017). Landslide displacement prediction using the GA-LSSVM model and time series analysis: a case study of Three Gorges Reservoir, China. *Nat. Hazards Earth Syst. Sci.* 17 (12), 2181–2198. doi:10.5194/nhess-17-2181-2017

Xu, Q. (2018). Constructing a new "three-check" system, innovating new mechanisms for disaster prevention and control. *China Min. Newsp.* Available at: https://www.93.gov.cn/xwjc-snyw/276052.html (Accessed June 07, 2024).

Xu, Q. (2020). Understanding and consideration of related issues in early identification of potential geo hazards. *Geomatics Inf. Sci. Wuhan Univ.* 45 (11), 1651–1659. (in Chinese with English abstract). doi:10.13203/j.whugis20200043

Xu, Q., Dong, X., and Li, W. (2019). Integrated space-air-ground early detection, monitoring and warning for potential catastrophic geohazards. *Geomatics Inf. Sci. Wuhan Univ.* 44 (7), 957–966. (in Chinese with English abstract). doi:10.13203/j.whugis20190088

Yao, C., Yao, X., Gu, Z., Ren, K., and Zhou, Z. (2022). Development law of active geological hazards in the Loess Plateau based on InSAR identification. *J. Geomechanics* 28 (2), 257–267. (in Chinese with English abstract). doi:10.12090/j.issn.1006-6616.2021083

Zhang, J., Tang, H., Li, C., Gong, W., Zhou, B., and Zhang, Y. (2024a). Deformation stage division and early warning of landslides based on the statistical characteristics of landslide kinematic features. *Landslides* 21 (4), 717–735. doi:10.1007/s10346-023-02192-7

Zhang, J., Tang, H., Tannant, D. D., Lin, C., Xia, D., Liu, X., et al. (2021). Combined forecasting model with CEEMD-LCSS reconstruction and the ABC-SVR method for landslide displacement prediction. *J. Clean. Prod.* 293, 126205. doi:10.1016/j.jclepro.2021.126205

Zhang, J., Tang, H., Zhou, B., Wen, T., and Zhang, S. (2024b). A new early warning criterion for landslides movement assessment: deformation Standardized Anomaly Index. *Bull. Eng. Geol. Environ.* 83 (5), 205. doi:10.1007/s10064-024-03672-3

Zhang, L., Liao, M., Dong, J., Xu, Q., and Gong, J. (2018). Early detection of landslide hazards in mountains areas of west China using time series sar interferometry try: a case study of danba, sichuan. *Geomatics Inf. Sci. Wuhan Univ.* 43 (12), 2039–2049. (in Chinese with English abstract). doi:10.13203/j.whugis20180181

Zhang, M., and Li, T. (2011). Triggering factors and forming mechanism of loess landslides. *J. Eng. Geol.* 19 (4), 530–540. (in Chinese with English abstract). doi:10.3969/j.issn.1004-9665.2011.04.014

Zhang, Q., Zhao, C., and Chen, X. (2022). Technical progress and development trend of geological hazards early identification with multi–source remote sensing. *Acta Geod. Cartogr. Sinica* 51 (6), 885–896. (in Chinese with English abstract). doi:10.11947/j.AGCS.2022.20220132

Zhang, S., Sun, P., Li, R., and Wang, F. (2023). Preliminary investigation on a catastrophic loess landslide induced by heavy rainfall on 1 September 2022 in Qinghai, China. *Landslides* 20, 1553–1559. doi:10.1007/s10346-023-02086-8

Zhang, S., Sun, P., Ren, J., Wang, H., Xin, P., and Wang, T. (2022). Successful emergency evacuation from a catastrophic loess landsli*de re*-activated by the torrential rain in October 2021 in Tianshui, Ganusu, NW China. *Geoenvironmental Disasters* 9 (1), 19. doi:10.1186/s40677-022-00222-5

Zhao, C., Liu, X., Zhang, Q., Peng, J., and Xu, Q. (2019). Research on loess landslide identification, monitoring and failure mode with InSAR technique in Heifangtai, Gansu. *Geomatics Inf. Sci. Wuhan Univ.* 44 (7), 996–1007. (in Chinese with English abstract). doi:10.13203/j.whugis20190072

Zhu, L., Hu, W., Zhang, M., Tang, Y., Bi, J., and Ma, J. (2013). An analysis of the soil mechanical properties involved in loess landslides in Heifangtai, Gansu Province. *Geol. Bull. China* 32 (6), 881–886. (in Chinese with English abstract). doi:10.3969/j.issn.1671-2552.2013.06.009